Universities of Leeds, Sheffield and York
http://eprints.whiterose.ac.uk/

Conditional Moment Closure Modelling of Soot Formation in Turbulent, Non-Premixed Methane and Propane Flames

ROBERT M. WOOLLEY

Energy and Resources Research Institute, School of Process, Environmental and
Materials Engineering, University of Leeds, Leeds LS2 9JT, UK
Telephone: +44 (0) 113 343 2351; Facsimile: +44 (0) 113 343 2405;
E-mail: r.m.woolley@leeds.ac.uk

MICHAEL FAIRWEATHER AND YUNARDI

Energy and Resources Research Institute, School of Process, Environmental and
Materials Engineering, University of Leeds, Leeds LS2 9JT, UK

Presented are results obtained from the incorporation of a semi-empirical soot model into a first-order conditional moment closure (CMC) approach to modelling turbulent, non-premixed methane- and propane-air flames. Soot formation is determined via the solution of two transport equations for soot mass fraction and particle number density, with acetylene and benzene employed as the incipient species responsible for soot nucleation, and the concentrations of these calculated using a detailed gas-phase kinetic scheme involving 70 species. The study focuses on the influence of differential diffusion of soot particles on soot volume fraction predictions. The results of calculations are compared with experimental data for atmospheric and 3 atmosphere methane flames, and propane flames with air preheated to 323 K and 773 K. Overall, the study demonstrates that the model, when used in conjunction with a representation of differential diffusion effects, is capable of accurately predicting soot formation in the turbulent non-premixed flames considered.

Keywords: *CMC; soot; methane; propane; differential diffusion.*

Nomenclature

d	diameter	D	diffusion coefficient
k	reaction rate constant or turbulence kinetic energy	M	molar mass
p	partial pressure	N	number or particle number density
r	radial distance or reaction rate		
u	axial velocity	P	probability density function
x	axial distance along centre-line	Q	transported scalar
A	surface area or pre-exponential factor	R	radius
		T	temperature
C	constant	Y	mass fraction

Greek symbols

ε	dissipation rate of k	σ	Stefan-Boltzmann constant
η	sample space variable	τ	characteristic time scale
κ	Boltzmann constant	φ	integration variable
ν	kinematic viscosity	χ	scalar dissipation
ξ	mixture fraction	w	production rate
ρ	density		

Subscripts

fv	soot volume fraction	ox	oxidation
g	growth	s	soot
h	enthalpy	A	Avogadro number
i	reactive scalar indice	K	Kolmogorov viscous scale
n	nucleation	R	radius

Superscripts

+	scalar of equal diffusivity	*	cross-stream averaged

Other symbols

$\langle \ \rangle$	ensemble averaging	$\langle \alpha \| \beta \rangle$	conditional expectation of α at some value β
$\{ \ \}_R$	integration over cross section limited by $\|r\| < R$	⊔	Favre average

## 1.	Introduction

Despite dwindling resources, fossil fuel combustion still plays a major role in the world economy and is widely used for the production of energy. The formation and emission of particulate pollutants such as soot, as a consequence of hydrocarbon combustion, is fast becoming a major concern in both developed and more so, developing countries. Soot generation usually results from incomplete combustion and typically occurs at fuel-rich stoichiometries. Although some of these particles are oxidized in the flame, soot that escapes oxidation is considered a serious environmental pollutant. There are also associated health risks since both polycyclic aromatic hydrocarbons (PAHs) that are precursors of soot and soot-associated organics have been identified to be carcinogenic. On the other hand, in cases where soot oxidation is completed within a flame, higher production of intermediate soot is desirable for increasing the radiant heat transfer from flames. Thus, control of soot production and reduction of soot emission from combustion processes are problems that need to be solved to obtain effective heat generation and to reduce harmful impacts to humans and the environment. Quantitative understanding of the soot growth and oxidation mechanisms in flames are critical to the development of approaches to control soot emissions.

Most practical combustion systems such as the gas turbine and internal combustion engine operate at high turbulence levels, with or without a combination of high pressure and preheated air. Consequently, it is important to numerically investigate soot formation under these conditions. While operation at elevated pressures proffers the significant advantage of increasing the thermodynamic efficiency of the system, it is also disadvantageous due to the releasing of more soot particles into the environment. The pressure dependence of soot formation and oxidation mechanisms is complicated,

and there is some evidence that they may be dissimilar for different pressure levels and hydrocarbon fuels. Although they are still not fully understood, it is widely accepted among researchers that increasing the pressure in the environment surrounding a non-premixed flame alters the reaction rate and the diffusion coefficients, which lead to the increase of soot production [1]. Most experimental studies of sooting processes to date have focussed primarily on laminar flames at atmospheric pressure and thus available data on soot levels in turbulent non-premixed flames at elevated pressures is very limited. Measurements in laminar [2, 3] and turbulent [4] non-premixed flames have shown that soot formation increases and soot oxidation decreases with increasing pressure. Brookes and Moss [4] argued that the increase of soot production from flames of 1 to 3 atm in pressure was due to the increase of the density and species concentrations (acetylene in particular), in the elevated pressure conditions, as well as the increase of soot residence time. In contrast to operation at high pressure which produces more soot, air preheating has been used as a means of reducing soot emissions and optimizing fuel consumption in practical combustors. As the air temperature becomes higher, the rates of some elementary reaction steps increase, while those of other elementary steps decrease. These changes affect the distribution of species and temperature across the flame as well as soot, CO, and NO emissions. A matter of concern in high-temperature air combustion is that of NO_x emissions. Experimental studies in to non-premixed methane flames [5, 6] have shown that as the temperature of incoming combustion air is increased, the NO_x emissions also increase. A major obstacle for further development of a combustion system with high efficiency and low soot emissions therefore appears to be the trade-off between the effects of elevated pressure and increased air preheat.

One of major challenges in turbulent combustion modelling involves accounting for interactions between turbulent flow and complex, finite-rate chemistry that are of profound importance when the prediction of minor chemical species and pollutants such as NO_x and soot is desirable. Significant progress has been made within the last two decades toward the development of combustion models capable of representing such interactions in turbulent combustion applications. Amongst those proposed, two appear to offer the most promising features for future development; these being the transported probability density function (PDF) approach [7] and the conditional moment closure (CMC) method [8]. Both achieve the goal of the inclusion of finite-rate chemistry into turbulent flow calculations, the former model doing so via the solution of a multi-dimensional transport equation of species and vector quantities, with solutions obtained by the implementation of a Monte Carlo technique. Although displaying very promising results in similar applications [9, 10], the method is computationally expensive, especially when the number of chemical species is large. At present, the deterministic CMC method provides a less restrictive approach to a wide range of practical applications, and can be easily integrated with a complex chemical kinetic scheme without requiring significant computer run times. Roomina and Bilger [11] investigated the application of CMC in modelling an attached turbulent methane flame and reported good agreement with data, with the exception to NO. Similar discrepancies in NO prediction were observed by Fairweather and Woolley [12, 13], who used a first-order CMC model to predict attached turbulent non-premixed flames of methane and hydrogen. Further investigation [14] revealed that by applying a second-order CMC closure to the chemical source term, improvement of NO predictions could be obtained. Calculations of lifted flames [15, 16] have also been made, with reasonable agreement obtained with experimental data. Kim et al. [17] compared the performance of the CMC

approach with that of the stationary laminar flamelet model when predicting the more complex flow of a bluff-body stabilized methanol flame, finding that CMC results provide superior agreement with data. In addition to these successes in modelling gas-phase combustion, CMC has previously shown promise in the calculation of soot formation in non-premixed flames [18].

In this paper, the results of an application of a first-order CMC approach [8] to the calculation of turbulent non-premixed flames and soot formation are presented. The soot model used in the calculations is based on that presented by Leung et al. [19] and Lindstedt [20], with transport equations for soot mass fraction and particle number density incorporated into the CMC approach. The influence of differential diffusion of soot particles in the context of CMC modelling, previously investigated by Kronenburg et al. [18], is further assessed within the computation of methane elevated pressure and propane preheated air flames. The turbulent flow field and CMC results in terms of mixture fraction, temperature, and soot volume fraction or soot concentration are validated against available experimental data [4, 21].

2. Mathematical modelling

2.1 Experimentally investigated flames

The non-premixed elevated-pressure methane, and preheated-air propane, flames considered in the present study were experimentally reported respectively by Brookes and Moss [4] and Nishida and Mukohara [21]. The methane-air flames [4] were studied at pressures of 1 and 3 atm. The flame was confined within a cylindrical pressure vessel with a length of 980 mm and internal diameter of 155 mm. A pure methane fuel issued from a cylindrical nozzle of a 4.07 mm in diameter with exit velocities of 20.3 and 6.77 m s^{-1} for the 1 and 3 atm flames, respectively. The jet flame was rim stabilized by an

annular premixed pilot flame, and a co-flowing air stream occupied the remainder of the inlet contained within the cylindrical liner. Temperature measurements were performed using fine-wire thermocouples and mean mixture fraction by microprobe sampling and mass spectrometric analysis. The mean soot volume fraction was measured by laser extinction tomography and reported at discrete flame heights of 300, 350, and 425 mm for the 1 atmosphere flame, and at 150, 200, 250, 300, and 350 mm for the 3 atmosphere flame. More details regarding the operating conditions of the methane flames investigated are presented in Table 1.

Two different propane-air flames [21] with combusting air temperatures of 323 K and 773 K were also investigated at atmospheric pressure. Propane at ambient temperature issued vertically upward into a combustion chamber with internal diameter of 115 mm and a length of 1 m from a burner nozzle having a diameter of 2 mm at an average velocity of 30 m s^{-1}. Air was supplied through an annulus surrounding the nozzle of diameter 105 mm, with average inlet velocities of 0.40 and 0.96 m s^{-1} being used for air preheat temperatures of 323 K and 773 K, respectively. A sampling probe method was used to measure the soot concentrations, whereas the flame temperature was measured with thermocouples coated with magnesium oxide. However, no correction due to radiation loss was made to the measured temperature data. In this study, the corrected temperature data as reported in Fairweather et al. [22] are employed, instead of uncorrected temperature data reported in Nishida and Mukohara [21]. Despite this problem of accounting for radiation errors with thermocouple measurements, they remain widely used for the establishment of temperature fields in combustion processes. Further details regarding the operating conditions of the propane flames investigated are given in Table 2.

With respect to non-premixed turbulent sooting propane jets, there are limited data available in the widely published literature against which model validations can be made. To the authors' knowledge, only two experimental studies provide sufficient information for modelling purposes, these being the previously discussed works of Nishida and Mukohara [21] and those of Jurng et al. [23]. The former study presents detailed measured profiles of soot concentrations along with gas temperature and species concentrations of two flames with differing inlet-air temperatures. Although flow-field data are not directly available, mixture fraction values may be extracted from information of local equivalence ratio. The latter study of Jurng et al. [23], although presenting data on the velocity field of a propane jet, does not provide information on species concentrations such as C_2H_2 which is of prime importance in the analysis of soot formation and growth during model development.

The measurement of the soot field in hydrocarbon flames is undertaken primarily by either sampling probe or optical techniques. A number of experimental investigations such as those conducted by Santoro et al. [24] have utilised the optical method of laser-light scattering/extinction techniques to determine the characteristics of soot formation and oxidation in non-premixed flames. Even though these techniques cause no disturbance to the system in which they are introduced, some of the assumptions required in applying these techniques are compounded by considerable uncertainties. One of these important assumptions is that the particle scattering intensities, which are proportional to the soot particle characteristics, are in the Rayleigh or Mie limit. Santoro et al. [24] measured soot particle size throughout a series of ethylene-air non-premixed flames using a Rayleigh method. From their measurements, it was observed that the largest particles have values close to 120 nm. Particles of this size are beyond the Rayleigh limit, the particle diameter being much less than the

wavelength of the scattered light. Therefore, the use of Rayleigh scattering procedures and theory seems inappropriate for this purpose. In his review paper, Kennedy [25] points out that the optical measurement results typically over-predict the sampling-probe technique results by approximately a factor of two. Therefore, one must exercise some caution in comparing modelling with experiments in light of the apparent uncertainty in the interpretation of the light extinction data. The sampling-probe technique on the other hand, provides directly computable local soot-particle characteristics. These methods have previously been used as an independent check on optical measurements due to their reliance upon basic physical principles. An obvious drawback to this technique is the disturbance of the system into which the probe is introduced. Also, problems can occur from soot deposition within the probe itself. Regarding this latter problem, Nishida and Mukohara [21] ejected N_2 gas from the probe tip to prevent such deposition when samples of the combusting gases were not being taken.

2.2   *Turbulent flow calculations*

The turbulent jet flames under consideration in this study are essentially parabolic and axisymmetric in nature. The calculation of flow and mixing fields was therefore achieved by solutions of the axisymmetric forms of the partial differential equations which describe conservation of mass, momentum and the transport of mixture fraction and its variance. For the variable density flows of interest, the Favre-averaged forms of these equations were employed. A standard *k-ε* turbulence model [26] was used to close the equation set. Closure of the mean density term was achieved using a prescribed β-PDF, with instantaneous values of density derived from adiabatic, equilibrium calculations based on the kinetic mechanism of Qin et al. [27]. Standard turbulence

modelling constants appropriate to axisymmetric flows were employed to ensure the accurate prediction of the spreading rate of the jets, apart from an adjustment made to the value of $C_{\varepsilon 2}$ from 1.92 to 1.84 used to increase the dissipation rate of turbulence kinetic energy. This form of adjustment has been used previously by a number of investigators [22, 28] to reduce the predicted spreading rate of such jets.

Solution of the two-dimensional, axisymmetric forms of the transport equations was achieved using a modified version of the GENMIX code, further details of which may be found in [12, 29]. Solution in axisymmetry used a symmetry plane along the centre-line of the jet issuing from the pipe, with the other lateral boundary a free boundary representing the co-flowing air stream. The only other boundary condition required, given the parabolic formulation, is at the upstream boundary, since outlet boundary conditions are produced as the solution of the integration process itself. Inlet boundary conditions for mean velocity and turbulence quantities were prescribed from experimental data. Numerical solutions were obtained using expanding finite-volume meshes, and in all cases grid-independent solutions were established using resolutions in excess of one million nodes. The distribution of these nodes was 300 in the radial direction, and upwards of 3500 in the stream-wise direction.

2.3 First-order CMC combustion model

When predicting turbulent combustion, difficulty is encountered in modelling the chemical source term that appears in the species transport equations. The highly non-linear dependence of this term on species concentrations and temperature, which fluctuate rapidly in turbulent flows, impedes any attempt at a linear first-order closure in terms of the averaged local temperature and concentrations. The first-order CMC method addresses this problem by utilising moments conditioned on a value of a

conserved scalar, namely the mixture fraction. Executing calculations in conserved scalar space removes much of the non-linearity of the chemical source term, resulting in smaller fluctuations away from the conditional mean [8].

A general first-order, one-dimensional, parabolic CMC equation can be obtained by averaging the instantaneous equation governing species mass fraction, Y_i, in statistically stationary, turbulent reacting flow, on the condition that the instantaneous mixture fraction ξ equals an arbitrary value η. However, experimental evidence has shown that there is a certain degree of non-negligible radial variation of the conditional moments across the width of flames such as these [30]. In order to account for any such variation that may be present, the CMC equation can be radially averaged by integrating across the flow [31]. When the conserved and reactive scalars have different diffusion coefficients, that is $D_i \neq D_\xi$, the unclosed form of the CMC equation can be written as:

$$\frac{\partial Q_i}{\partial x}\langle u|\eta\rangle^* = \frac{1}{2}\frac{D_i}{D_\xi}\langle \chi|\eta\rangle^* \frac{\partial^2 Q_i}{\partial \eta^2} + \left(\frac{D_i}{D_\xi}-1\right)\left\langle \frac{\partial}{\partial x}\left(\rho D_\xi \frac{\partial \xi}{\partial x}\right)\middle|\eta\right\rangle^* \frac{\partial Q_i}{\partial \eta} + \langle w_i|\eta\rangle + e_{y,i} \quad (1)$$

In this equation, $\langle ...|\eta\rangle^*$ denotes a term which is not only averaged on the condition that the local mixture fraction ξ is equal to a value η, but it is also integrated across the flow. The term in angular brackets on the left side of Eq. (1) represents the conditional axial velocity, modelled as a PDF-weighted cross-stream averaged value defined as:

$$\langle u|\eta\rangle^* \equiv \frac{\{u(r)P(\eta,r)\}_R}{\{P(\eta,r)\}_R} \quad (2)$$

where $\{...\}_R$ denotes cross-stream averaging, defined as $2R^{-2}\int_0^R (...)r\,dr$, with R a characteristic radius. The first term in angular brackets on the right-hand side of Eq. (1) represents the conditional scalar dissipation, and its accurate modelling is of vital importance, especially near the reaction zone where $\partial^2 Q_i / \partial \eta^2$ is significant [8].

Solution of the equations for the mixture fraction and its variance, and the assumption of an assumed form of the mixture fraction PDF at each radial location allows the calculation of this conditional mean scalar dissipation rate. Barlow et al. [32] compared both a clipped Gaussian and a β-PDF formulation in their calculations, and found the differences between the resulting profiles to be small. Following Girimaji [33], the β-function is used herein, and the conditional mean scalar dissipation rate is modelled as:

$$\langle \chi | \eta \rangle = -2\tilde{\chi} \frac{\tilde{\xi}(1-\tilde{\xi})}{\left(\widetilde{\xi''^2}\right)^2} \frac{I(\eta)}{\tilde{P}(\eta)} \tag{3}$$

where

$$I(\eta) = \int_0^\eta \left\{ \tilde{\xi} \left[\ln \varphi - \langle \ln \eta \rangle \right] + (1-\tilde{\xi}) \left[\ln(1-\varphi) - \langle \ln(1-\eta) \rangle \right] \right\} \tilde{P}(\varphi)(\eta - \varphi) d\varphi \tag{4}$$

and the unconditional Favre mean scalar dissipation rate $\tilde{\chi}$ is defined from the conventional equality of time scales for the velocity and mixture fraction, with the constant $C_{\tilde{\chi}} = 2.0$, as:

$$\tilde{\chi} = C_{\tilde{\chi}} \frac{\varepsilon}{k} \widetilde{\xi''^2} \tag{5}$$

Although Girimaji's model was developed for isotropic turbulence, validation of its implementation has been successfully performed in a number of non-premixed jet flame calculations using the CMC approach [12, 13].

For the derivation of the conditional gas-phase species mass fraction equations, it is assumed that both reactive and conserved scalars diffuse equally, which implies $D_i = D_\xi$. With this assumption, the second and last terms on the right hand-side of Eq. (1), representing the source terms that generate differential and spatial diffusion respectively, are cancelled. The remaining non-linear chemical source term $\langle w_i | \eta \rangle$ is modelled as for simple first-order closure. Mean values were obtained using the

CHEMKIN package [34] together with a full chemical kinetic scheme consisting 70

species and 463 reactions attributed to Qin et al. [27] and optimised on the oxidation of

C_3 hydrocarbon species. The C_1 and C_2 kinetic components were obtained from the

GRI-Mech 3.0 mechanism [35], and propane chemistry represented by 258 additional

reactions from the scheme of Davis et al. [36]. Although this mechanism is focussed

upon propane combustion, its predictive ability with regards to laminar flame speed and

shock-tube ignition delay was successfully tested against CH_4, C_2H_4, C_2H_6, C_3H_4, and

C_3H_6, in addition to C_3H_8. The mechanism incorporates reactions which lead to the

formation of the cyclic polyaromatic hydrocarbons benzene and phenyl. Reaction

pathways with the PAH precursor acetylene were well represented, and the important

formation paths of benzene through reactions involving C_2H_2, C_3H_3, n-C_4H_3, and n-

C_4H_5 are also applied. These inclusions form the basis of the chemistry scheme used in

the present work. Prior to its implementation in the sooting flame calculations, tests

were undertaken to establish its performance in the prediction of conditional major and

minor species in non-sooting methane flames, with results comparable to those obtained

using the GRI-Mech 3.0 [35] and Miller and Bowman [37] mechanisms.

The evolution of soot particles in a non-premixed turbulent flame is strongly

coupled to its radiative heat transfer, with soot formation and oxidation strongly

influenced by the temperature. It is therefore necessary to include the influence of

energy loss due to radiation in the conditional mean equation for enthalpy:

$$\frac{\partial Q_h}{\partial x}\langle u|\eta\rangle = \frac{1}{2}\langle \chi|\eta\rangle\frac{\partial^2 Q_h}{\partial \eta^2} + \langle w_h|\eta\rangle \qquad (6)$$

In this work, a simple radiation model was employed, where emissions from species

CO_2, H_2O, CH_4, CO and soot were included. The model, based on that of Maracino and

Lentini [38], gives the conditional radiation heat loss source term in Eq. (6) as:

$$\langle w_h | \eta \rangle = -4.0\sigma \left[p \langle T | \eta \rangle^4 \sum_i a_i \langle T | \eta \rangle Q_i + a_s Q_{fv} \langle T | \eta \rangle^5 \right] \tag{7}$$

Values of the Plank mean absorption coefficients for gaseous species (a_i) were calculated in accordance with Maracino and Lentini [38], with the value for soot (a_s) taken to be = 2370 m^{-1}K^{-1} [39].

Flow field information from the turbulent flow calculations employing a reacting flow density was passed to the CMC model, where the set of species mass fractions, soot mass fraction and particle number density, and enthalpy equations were solved. Comparison between densities obtained from the CMC solution and prescribed equilibrium values showed little variation, such that coupling of the flow field and CMC calculations was deemed unnecessary. Solution of the CMC equations in real space was achieved using a fractional step method, implemented using the stiff ODE solver VODE [12, 40]. The number of grid nodes used in the CMC calculation was established from earlier works [12-14], with 68 nodes in mixture fraction space proving to be adequate to prevent numerical error. The complete calculations for each flame took less than 4 hours on a single dedicated 900 MHz UltraSparcIIIcu central processor with up to 24 GB of shared physical memory per calculation.

2.4   Soot formation model

Although different approaches have been proposed to model soot formation in combustion processes, no single universal model is currently available. A detailed soot model such as that proposed by Frenklach and co-workers [41, 42] expands the applicability of soot predictions in various ranges of conditions. The model basically consists of two parts: a detailed gas-phase reaction mechanism describing soot chemistry; and a model for the aerosol particle dynamics which includes statistical

treatments of simultaneous particle nucleation, coagulation of particles, surface condensation, surface growth and oxidation. However, the accuracies of such detailed soot models are dependent on the inception, surface growth and surface condensation mechanisms, and their present use is impaired by poor representation of soot inception chemistry [43]. Further, these models are expensive in terms of CPU time, even when undertaking simulations of laminar flames. Thus, for predictions of soot in practical engineering equipment, it is often necessary to use simplified models to keep calculation time to an acceptable level. The soot model developed by Lindstedt and co-workers [19, 20] has been successfully applied in previous studies for the simulation of both laminar and turbulent non-premixed flames of different fuels [18, 22]. The model incorporates many aspects of the physics and chemistry of soot formation and oxidation, including nucleation, soot mass growth, agglomeration, and soot oxidation steps. Simplification is achieved by expressing the rates of soot nucleation and growth with one- or two-step reactions. Particle dynamics are modelled through solution of two transport equations for soot mass fraction and particle number density. Moss and co-workers [44, 45] also developed a similar two-equation approach. Although both these models are based upon the same physical foundation, they differ in model parameters and constants. Both models have been used in predictions of soot in turbulent non-premixed sooting flames operated at elevated pressure and preheated air, but in the present study, soot formation is modelled in the manner prescribed by Leung et al. [19] and Lindstedt [20]. Soot nucleation in the original Leung et al. [19] model was entirely related to acetylene as the only incipient species, and the original nucleation model provides good agreement for simple fuels, but is less satisfactory for more complex cases. In a later development, soot nucleation was assumed to result not only from a first-order acetylene reaction but also a benzene reaction [20]:

$$C_2H_2 \square \quad 2C_s + H_2 \tag{8}$$

$$C_6H_6 \square \quad 6C_s + 3H_2 \tag{9}$$

The reaction rate for nucleation is approximated by first-order terms for these species:

$$r_n = 2k_1(T)[C_2H_2]M_s + 6k_2(T)[C_6H_6]M_s \tag{10}$$

where M_s is the molar mass of soot, taken to be 12.011 kg kmol^{-1}. The soot mass

growth is assumed due to the adsorption of acetylene on the surface of a soot particle,

following a reaction similar to Eq. (8). The surface growth reaction rate is given by:

$$r_g = 2k_3(T)f(A_s)[C_2H_2]M_s \tag{11}$$

where $f(A_s)$ is a function of the total surface area per unit volume of mixture. In this

work, it is assumed that the function $f(A_s)$ is proportional to the soot surface area A_s,

i.e. $f(A_s) = A_s$. Assuming spherical particles, the soot particle diameter d_s is related to

soot mass fraction Y_s and particle number density N_s through:

$$d_s = \left(\frac{6}{\pi}\frac{Y_s}{\rho N_s}\right)^{1/3} \tag{12}$$

The soot surface area per unit volume may now be expressed as:

$$A_s = \pi \left(\frac{6}{\pi}\frac{Y_s}{\rho N_s}\right)^{2/3} \rho N_s \tag{13}$$

Oxidation of soot occurs at the particle surface as a result of attack by molecular oxygen

and the hydroxyl radical, although under some circumstances the O atom and other

oxygenated species such CO_2, H_2O and NO_2 may be important [46]. In this work, soot

oxidation is assumed to occur through O_2 and OH, with the following reaction steps:

$$C_s + \frac{1}{2}O_2 \rightarrow CO \tag{14}$$

$$C_s + OH \rightarrow CO + H \tag{15}$$

The soot oxidation rate then takes the form:

$$r_{ox} = k_4(T) A_s [O_2] M_s + k_5(T) A_s [OH] M_s \tag{16}$$

Hence, the conditional source term for the soot mass fraction can be expressed as:

$$\langle w_{Y_s} | \eta \rangle = 2k_1(Q_T) Q_{C_2H_2} M_s + 6k_2(Q_T) Q_{C_6H_6} M_s + 2k_3(Q_T) A_s Q_{C_2H_2} M_s$$
$$- k_4(Q_T) A_s Q_{O_2} M_s - k_5(Q_T) A_s Q_{OH} M_s \tag{17}$$

The nucleation steps also give rise to the source term in the conservation equation for number density. It is assumed that the decrease in particle number density is due to particle agglomeration, modelled using a normal square dependence. The conditional source term for soot particle number density can thus be written as:

$$\langle w_{N_s} | \eta \rangle = \left[2k_1(Q_T) Q_{C_2H_2} + 6k_2(Q_T) Q_{C_6H_6} \right] \frac{N_A}{C_{min}}$$
$$- 2C_a \left(\frac{6}{\pi} \frac{Q_{Y_s}}{\rho_\eta Q_{N_s}} \right)^{1/6} \left(\frac{6\kappa Q_T}{\rho_s} \right)^{1/2} \left(\rho_\eta Q_{N_s} \right)^2 \tag{18}$$

where N_A is the Avogadro Number (6.022 x 10^{26} kmol^{-1}) and C_{min} the number of carbon atoms in the incipient soot particle, taken as 60 in this study [20]. κ is the Boltzmann constant, (1.38 x 10^{-23} J K^{-1}) and C_a is the agglomeration constant having a value in the range 3-9 [20, 47]. A value of 9 for this constant was employed in this work. The density of soot ρ_s was taken as 2000 kg m^{-3}. Reaction rate constants for nucleation, surface growth and oxidation are presented in Table 3.

In addition to the CMC transport equation for the gas-phase species, the soot model requires the solution of two additional transport equations for the soot mass fraction, Y_s, and the soot particle number density, N_s. In the case of differential diffusion being neglected, the transport equations for Y_s^+ and N_s^+ are obtained in a

similar way as for the gas-phase species, setting $D_{Y_s^+} = D_{N_s^+} = D_\xi$ for $i = Y_s^+, N_s^+$ in Eq. (1), giving:

$$\frac{\partial Q_{Y_s}^+}{\partial x} \langle u|\eta \rangle^* = \frac{1}{2} \langle \chi|\eta \rangle^* \frac{\partial^2 Q_{Y_s}^+}{\partial \eta^2} + \langle w_{Y_s}|\eta \rangle \tag{19}$$

$$\frac{\partial Q_{N_s}^+}{\partial x} \langle u|\eta \rangle^* = \frac{1}{2} \langle \chi|\eta \rangle^* \frac{\partial^2 Q_{N_s}^+}{\partial \eta^2} + \langle w_{N_s}|\eta \rangle \tag{20}$$

where the superscript + refers to a scalar of equal diffusivity. When the differential diffusion of soot particles is taken into account, fixing the molecular coefficients of soot particles and nuclei equal to zero, i.e. $D_{Y_s} = D_{N_s} = 0$ for $i = Y_s, N_s$, Eq. (1) can be simplified by neglecting the dissipation term. However, the last term on the right hand side of Eq. (1), $e_{y,i}$, cannot be neglected and requires modelling. This term represents the spatial diffusion of conditional fluctuations of species Q_{Y_i} [8], and Kronenburg and Bilger [48, 49] investigated and developed a closure for this term in turbulent non-premixed reacting flows with the aid of DNS, modelling it as:

$$e_{y,i} = -0.4 \frac{\left(Q_i - Q_i^+ \right)}{\tau_K} \tag{21}$$

where τ_K is the Kolmogorov time scale defined as $\tau_K(\eta) = [\nu(\eta)/\varepsilon(\eta)]^{1/2}$. The kinematic viscosity of the gas mixture is calculated from its composition and temperature, and the energy dissipation rate is obtained from the turbulent flow field calculation. Again, PDF-weighted cross-stream averaged values were implemented for these terms, and the transport equations that account for differential diffusion of soot particles can be obtained by substituting Eq. (21) into Eq. (1) for $i = Y_s, N_s$ to give:

$$\frac{\partial Q_{Y_s}}{\partial x} \langle u|\eta \rangle^* = -\left\langle \frac{\partial}{\partial x}\left(\rho D_\xi \frac{\partial \xi}{\partial x} \right)\middle|\eta \right\rangle^* \frac{\partial Q_{Y_s}}{\partial \eta} + \langle w_{Y_s}|\eta \rangle - 0.4 \frac{\left(Q_{Y_s} - Q_{Y_s}^+ \right)}{\tau_K(\eta)} \tag{22}$$

$$\frac{\partial Q_{N_s}}{\partial x}\langle u|\eta\rangle^* = -\left\langle\frac{\partial}{\partial x}\left(\rho D_\xi \frac{\partial \xi}{\partial x}\right)\Big|\eta\right\rangle^* \frac{\partial Q_{N_s}}{\partial \eta} + \left\langle w_{N_s}|\eta\right\rangle - 0.4\frac{\left(Q_{N_s} - Q_{N_s}^+\right)}{\tau_K(\eta)} \tag{23}$$

The source terms $\left\langle w_{Y_s}|\eta\right\rangle$ and $\left\langle w_{N_s}|\eta\right\rangle$ which appear in Eqs. (19), (20), (22) and (23)

are closed using Eqs. (17) and (18), and the first terms on the right-hand side of the

latter two equations, representing molecular diffusion, are modelled as [8]:

$$\left\langle\frac{\partial}{\partial x}\left(\rho D_\xi \frac{\partial \xi}{\partial x}\right)\Big|\eta\right\rangle = \frac{\partial\langle\chi|\eta\rangle}{\partial\eta} \tag{24}$$

thereby maintaining conformity with the prescription of the PDF equation and of the

scalar dissipation.

3.   Results and discussion

3.1   *Methane-air elevated pressure flames*

The results of the CMC calculations are compared within available data for the 1 and 3

atmosphere flames [4] in Figs. 1 and 2, respectively.   In addition to the centre-line

profiles, Fig. 1 also presents predicted and measured values of the radial mixture

fraction and temperature at five different heights above the burner for the atmospheric

methane flame. The predicted mixture fraction decay along the centre-line of the jet is

generally well reproduced by the *k-ε* turbulence model.   It is well known that the

standard *k-ε* turbulence model over-predicts the spreading rate of a round jet, and the

modification performed by reducing $C_{\varepsilon 2}$ from 1.92 to 1.84 results in improved

predictions. These more closely matched the dataset, with the exception being in the

region between 100 to 200 mm.   In this region, the centre-line mixture fraction

predictions are slightly lower than those measured. In contrast, Kronenburg et al. [18],

employing a *k-ε-g* turbulence model, somewhat over-predicted the axial mixture

fraction in the region up to 200 mm above the nozzle. Turning to the radial profiles,

predictions of mean mixture fraction are generally in good agreement with data, except for under-prediction at the edges of the flames at the 150, 300 and 350 mm locations. Such discrepancy might be due to some uncertainty relating to mixture fraction measurements taken by probe sampling in these fuel-lean regions at the edges of the flames caused by carbon retention in the sampling line [4].

The centre-line temperature predictions in the 1 atm flame generally display qualitatively and quantitatively good results in comparison to the experimental data. It should be noted that the flat calculated axial temperature profile close to the nozzle indicates a region prior to CMC calculations commencing. It is seen that the progress of the computed temperature is in line with the measurements, aside from the region between 150 and 250 mm above the nozzle where the temperature is marginally over-predicted, but by less than 150 K. The apparent form of the data in the range noted above could well be consequential of using thermocouples, with temperature measurements being difficult to perform in the core of a sooting flame, as noted by Mauss et al [50]. However, outside this range the temperature is in good agreement with data. The experimental data indicates that the flame tip, where the mean mixture fraction is at its approximate stoichiometric value and temperature at its peak, is about 425 mm downstream, with the temperature at this height correctly predicted.

With respect to the radial temperature profiles, predictions are in good agreement at heights of 150 and 200 mm. Consistent with the axial temperature prediction, differences of less than 10% are observed along the axis of the flame at x = 200 mm. Although the temperature profile in fuel-rich regions, and peak temperature locations, are satisfactorily reproduced at all flame heights, the spreading of the flame is less well represented, with temperature predictions in the fuel-lean region falling below measured values, particularly for flames above 250 mm. Weakness in the k-ε turbulence model

and neglect of conditional turbulence fluctuations are believed to be mainly responsible for this poor performance in the calculations.

Shown in Fig. 2 are predicted and measured results of axial and radial temperatures of the 3 atm flame, where the trend of temperature evolution along the centre-line can be seen to be well captured by the CMC model. The centre-line temperature is predicted well in the region near the burner, but slightly over-predicts further downstream. Comparing the centre-line profiles of the 1 atm and 3 atm flames, it is seen that the latter flame has a lower peak temperature. This can be attributed to the increased radiative heat loss from the 3 atm flame due to the increased soot volume fraction. Both experiment and prediction indicate that the flame height in the 3 atm flame is about half that of the 1 atm flame, as indicated by the spatial location of the peak temperatures. This is a consequence of maintaining the same fuel mass flow rate in both flames which effects a velocity decrease from 20.3 m s^{-1} to 6.77 m s^{-1} as the pressure increases from 1 to 3 atm.

Inspection of radial temperature profiles indicates that the flame width at 200 mm downstream is somewhat under-predicted. A comparable discrepancy was also observed by Kronenburg [18] using a similar combustion model. The source of this discrepancy is possibly the inaccurate prediction of the mixing of the jet by the flow field model. However, neither experimental axial or radial mixture fraction data are available to make comparison with predictions. At all measurement locations, the predicted temperatures at the axisymmetric boundary deviate by up to 15% from the experimental values, being consistent with the observations made of the centre-line temperature profile. At heights of 100 and 150 mm, the predicted temperature profiles and their peaks are in good agreement with data, but less so at 200 mm. This level of agreement between measured and predicted temperature is comparable to that observed

by Kronenburg et al. [18]. With a difference of less than 5% in peak temperature predictions in both the 1 and 3 atm flames, as shown in Fig.1 and Fig. 2, the method of accounting for soot radiation is considered satisfactorily implemented in these flames.

Due to the nature of methane-air flames, which produce relatively low levels of soot, particularly at atmospheric pressure, and the difficulty of accurately recording such levels, soot volume fraction measurements were performed only at heights of 300, 350 and 425 mm above the nozzle in the 1 atm flame. Axial and radial variations of soot volume fraction are compared for this flame in Fig. 3. It may be noted that, in terms of the centre-line measurements, high soot volume fractions are observed within the soot formation region but, unfortunately, soot volume fraction data in the soot oxidation regions are not available. The solid line in this figure represents the simulations resulting from considering the effect of differential diffusion, and the dashed line the simulations which neglected differential diffusion in the CMC calculation. With the assumption of equal diffusivity applied, it is evident that the centre-line soot volume fraction profile is significantly under-predicted in both the soot formation and oxidation zones. The predicted soot formation starts at a lower flame height than when differential diffusion is accounted for, leading to a three-fold under-prediction of peak soot volume fraction. A key issue is the discrepancy between the computed and measured soot volume fraction in the formation zone being directly related to the modelling of the surface growth rate in the soot model. When the effect of differential diffusion is neglected, the approximation that the surface growth rate is proportional to the local soot surface area, $f(A_s) = A_s$, results in low soot volume fractions, as observed by Kronenburg et al. [18] in similar methane flames, and Lindstedt [20] and Ma et al. [28] in ethylene flames.

If the differential diffusion between soot particles and gas-phase species is taken into account, the first term on the right hand side of Eqs. (22) and (23), the diffusion term, is responsible for transporting soot particles from lower to higher mixture fraction regions [18], causing an increase in soot mass fraction in soot formation regions. Higher soot mass fractions provide larger soot surface areas which lead to enhanced soot formation rates. It is therefore not surprising to discover that the soot volume fraction prediction in the formation zone is in line with measurements when differential diffusion is considered in the CMC model. The magnitude of the peak soot volume fraction is 18% below the measured value, and its spatial position is 8% lower than the experimental measurement. Brookes and Moss [4] have, however, pointed out four principal sources of error in the measured soot volume fractions. These originate from measurement of the mean extinction profile, selection of the value of refractive index, application of the Rayleigh limit, and the assumption that the soot particles are spherical. A deviation of less than 20% in the current prediction is therefore reasonably acceptable since experimental error of approximately ±50% in the mean soot measurement could result from a combination of all the above sources. Results for the centre-line soot volume fraction were found to be comparable to those of previous investigations [18] which also used the soot model of Leung et al [19].

Inspection of the radial profiles of soot volume fraction at all downstream locations, also shown in Fig. 3, indicates that poor agreement between prediction and measurement is obtained with the assumption of equal diffusivity. Results based on the differential diffusion model, however, are much improved. At a position of 300 mm above the burner, the soot level in the fuel-rich region is notably over-predicted, and at the core is approximately 50% greater than the experimental observation. Further away from the centre-line the discrepancies between the measured and predicted soot volume

fractions diminish. The radial plot illustrates a peak in the soot volume fraction located off-axis which is not seen in the experimental values. At all axial locations, the radial profiles of soot volume fraction fall quickly towards the edge of the flame, as clearly seen at x = 350 and 425 mm. Nonetheless, the key trends in the soot evolution with downstream distance are captured by the computed profiles. The experimental data do, however, show a sooting region which is growing radially with downstream distance, whilst the predictions are of a nearly constant width at all axial locations. Previous predictions [18, 51] were also unable to correctly capture this experimentally observed growth of the sooting zone, particularly at the last two axial locations.

In contrast to the 1 atm flame, soot measurements in the higher pressure flame provide a more comprehensive picture of soot formation and burn-out, as data for soot volume fractions are distributed at five different axial positions. From the axial profile shown in Fig. 4, the soot formation within the flame occurs in regions where fuel-rich conditions dominate, with the bulk of the soot volume fraction being concentrated in mid-flame regions, between 200 and 300 mm. In comparison to the 1 atm flame, soot production in the 3 atm flame is increased by approximately an order of magnitude. The calculated centre-line soot volume fraction again shows that improved predictions can be achieved by incorporating the differential diffusion effects of soot particles into the CMC model. Soot volume fraction distribution is qualitatively and quantitatively in excellent agreement with measurements when such effects are accounted for, in both the soot formation and oxidation zones. The formation of soot has already been seen in the core of the flame at a height of 50 mm, and the predictions grow steadily, consistent with experimental observations, until reaching a maximum value at 240 mm. The prediction of soot decay due to oxidation is also well represented, indicating the assumption that soot oxidation due to the attack of the OH radical and molecular O_2

yields accurate results. The overall accurate prediction of the growth, peak and subsequent decay of centre-line soot volume fraction indicates that the balance between soot formation and oxidation is reproduced well. This is expected since the enhanced soot production in the 3 atm flame permits more accurate soot measurement than in the corresponding data of the 1 atm flame. In comparison to the predictions of earlier studies, Kronenburg et al. [18] correctly predicted the soot variation in the formation region of this flame, but slightly under-predicted in the oxidation zone. In addition, Brookes and Moss [52] under-predicted and over-predicted soot levels in the formation and oxidation zones, respectively.

The numerical predictions from this study demonstrate an increase of soot production with increased pressure, in line with experimental evidence [2-4]. However, there has been no comprehensive explanation regarding the mechanisms responsible for such an increase. Although it is believed that both physical and chemical effects play important roles in soot formation at high pressure, a number of numerical simulation studies show that the influence of pressure is primarily a physical phenomenon rather than a chemical one. Roditcheva and Bai [51] argued that in addition to the increase of density and soot precursor species concentrations, which result in an increase of soot surface growth rate, the increase of residence time also contributes by giving allowance to the relatively slow soot chemistry. However, Liu et al [53] confirmed from their simulations that soot particles experience almost the same residence times at different pressures. Zhang and Ezekoye [54] suggested that enhanced soot production at increased pressure can be attributed simply to the increased mixture density, which is proportional to pressure. As a result, the acetylene concentration is also increased proportionally to pressure due to its linear dependence on mixture density. This is

supported from results obtained in this study, which exhibit a significant increase of

acetylene species concentration as pressure is increased from 1 to 3 atm.

An evaluation of the CMC-soot model with respect to radial profiles of soot

volume fraction in the 3 atm flame is also presented in Fig. 4. At all axial locations, the

predicted soot levels deviate considerably from the experimental trends when

differential diffusion is neglected in the calculation. With the inclusion of differential

diffusion effects, quantitative and qualitative improvements in predictions are

noticeably seen, with results at the first three axial locations providing best agreement

with the experimental data. At the position of 150 mm above the burner, the calculated

off-axis peak soot volume fraction is around 30% higher than the experimental value,

although greater discrepancy was found in previous works [18]. The calculated soot

volume fraction at the two last locations in the flame is under-predicted, which is

possibly a consequence of inaccurate temperature predictions. This contrasts to the

flamelet predictions of Roditcheva and Bai [51] which accurately simulate the radial

temperature profile at all axial locations, but imprecisely compute the radial soot yields.

Employing Moss' soot model [44, 45], they generally under-predicted soot volume

fractions at all axial locations, with an exception at x = 350 mm. The best accord

between the data and calculations was obtained when the surface growth constant was

adjusted from 0.075 to 0.085. It is important to note here that no adjustment was made

in this study, either to the soot growth or oxidation rate to achieve the current level of

agreement in both axial and radial profiles of soot volume fraction.

3.2 *Propane-air preheated flames*

Fig. 5 presents profiles of predicted centreline mean mixture fraction, plotted against

experimental data for both the 323 K and 773 K preheated-air flames. The experimental

data were obtained from the axial profile of local equivalence ratio, subsequently obtained from the measured gas concentrations, and the solid and dashed lines correspond to predictions of the 323 K and 773 K preheated-air flames respectively. It is observed that the computed axial mixture fraction predictions for both flames is in good agreement with the experimental data, which indicates that the mixing fields of both the propane-air flames are well represented by the applied k-ε turbulence closure. Drawing comparison with predictions made of the methane-air flow-fields, the current calculations appear to be more conforming with experimental evidence and are hence accepted to be of sufficient accuracy to base the chemistry models upon.

The source terms in Eqs. (19) and (20) for soot mass fraction and soot particle number density are highly dependent upon the temperature, soot inception, growth, and oxidative species concentrations, and the accurate prediction of these scalars is of prime importance to the performance of the CMC-soot model. The predicted axial and radial distributions of temperature for the 323 K and 773 K preheated propane-air flames are compared with experimental data in Figs. 6 and 7. Centre-line mean temperature predictions of the two flames are not as satisfactory compared with the previous calculations, although the temperatures in the mid-flame region and its peak are well represented. Over-predictions are observable in the upstream regions close to the burner between 100 and 350 mm for the 323 K, and 100 to 300 mm for the 773 K, preheated-air flames. As in the case of the methane-air flames, these discrepancies may be due to the uncertainty of temperature measurement in the core of a sooting flame which is difficult to perform using thermocouples. Under-predictions are observed in the regions further downstream which is likely due to short-comings of the radiation model employed. The type of radiation model employed has been found to yield reasonable accuracy in many non-sooting combustion applications [12, 13], and its

application, when extended to account for soot radiation, also yields reasonable agreement in the low sooting methane flames investigated in this study. In the presence of relatively high concentrations of soot, as in the case of the propane flames, its performance is perhaps questionable. However, in view of the radial temperature predictions, described below, the radiation model employed would appear to be capable of yielding reasonable estimations of flame temperatures.

Radial temperature profiles along with measurements for the two cases studied are also depicted in Figs. 6 and 7. In general, these predictions are in good agreement with the experiments. The flame width is slightly over-predicted in the upstream and somewhat under-predicted further downstream in the lower preheat temperature case. It is, however, very well represented in the case of 773 K preheated-air flame, apart from at 400 mm downstream. Consistent with the centre-line temperature prediction, the temperatures at the core of the flame are over-predicted at axial positions of 100, 200 and 300 mm for the 323 K flame, and 100 and 200 mm for the 773 K flame, although closer to the nozzle, off-axis peak temperatures are correctly predicted. The spreading-rate of the flames seems to be slightly underestimated at further downstream positions, with the temperature predictions in the fuel-lean regions falling below the measurements. Nonetheless, the level of agreement of the radial temperature profile in both cases investigated is comparable to that obtained by Fairweather et al [22] and Coelho and Carvalho [55] who employed a steady laminar flamelet approach.

The centre-line growth and decay of soot levels within both flames, in addition to their radial profiles, is presented in Figs. 8 and 9. Again, it is evident in both axial and radial profiles that the neglect of differential diffusion effects leads to a substantially low soot yield. In contrast, the soot concentration predictions are brought in line with experimental findings when differential diffusion is accounted for.

Subsequent discussion is based on the results obtained with the consideration of differential diffusion.

The calculated centre-line evolution for the lower-air temperature flame, shown in Fig. 8, reveals that the soot concentration grows at a slower rate than is observed experimentally up to 200 mm above the burner tip. This is partly due to an under-prediction of acetylene levels within this region (not shown). The predicted soot levels in the oxidation region are in good agreement with the data up to 550 mm, but fall below the measurements further downstream which may be attributed to inaccurate temperature prediction within this region. A similar discrepancy was also observed in previous studies [28, 55], and Fairweather et al. [22] adjusted the soot oxidation rate by one half in order to bring the soot predictions further downstream in line with experiment. Without any adjustment being made to the soot model in the present work, however, the agreement of soot growth and destruction within the 323 K flame may be considered very good.

Although similar behaviour is observed in the higher temperature preheated-air flame, as illustrated in Fig. 9, the rate of increase in the soot formation zone is much slower, leading to under-predictions of soot levels over this region. This discrepancy forces a downstream shift of the overall shape from the measured profile. As a result, the soot levels in the oxidation zone are higher than the measured values, implying the predicted soot oxidation rate is lower than observed in the experiment. However, such a conclusion is misleading since the balance between soot formation and oxidation throughout the flame is well represented. Atomic oxygen is considered an important oxidant of soot at higher temperatures [46], but its incorporation into the current soot oxidation expression did not have a notable influence upon the predictions.

Uncertainties in soot concentration measurements, obtained using probe techniques, or errors in flow field predictions, may be responsible for this shift.

Analysis of the position of peak soot concentration may also explain the downstream shift of the soot profile in the 773 K flame. Both on the centre-line and radially, the maximum soot levels are located at approximately stoichiometric conditions where the temperature is at its peak. Inspection of experimental data in Figs. 8 and 9 reveals that the centre-line peak soot concentration is at 250 mm above the nozzle for both the 323 K and 773 K flames. However, at this position, as seen in Figs. 6 and 7, the temperature is far from its maximum value since the 323 K and 773 K flames reach a maximum temperature at around 400 mm and 350 mm, respectively. Turning to the calculated soot profiles, the soot reaches its peak value of 2.27 g Nm^{-3} at 360 mm above the nozzle for the 323 K flame, and of 3.25 g Nm^{-3} at 300 mm for the 773 K flame. Both these locations are in reasonable accord with the experimental maximum temperature positions as well as the predicted maximum temperature positions of 370 and 310 mm for the lower and higher temperature preheated-air flames respectively. This implies that important features in the two flames investigated are adequately described by the CMC-soot model.

Radial profiles of predicted and measured soot levels at different axial locations in the 323 K and 773 K flames are also shown in Figs. 8 and 9. In agreement with the predicted axial profile at a position of 100 mm, the soot concentrations close to the axis are negligible and, although observed levels are not predicted, the off-axis soot peaks are captured. Examination of radial acetylene profiles near the axis of both flames at the same height (not shown) reveals that its concentrations are under-predicted, but not zero. Consequently, under-prediction in acetylene appears to provide a relatively small contribution to this discrepancy, and further investigation is required on other factors,

such as turbulent fluctuations, which may contribute to this inconsistency. Beyond the axial position of 100 mm, the model improves in predictions of soot levels in fuel-rich regions. However, in most locations, the destruction rate of the soot particles in the radial direction, towards the edge of the flame, is slightly under-predicted for both cases.

At this point, it is considered that some discussion regarding the performance of the model in mixture fraction space may be informative to the reader. Hence, Fig. 10 is presented, which illustrates the evolution of conditional mean soot concentrations in mixture fraction space at three different axial locations for the 323 K and 773 K preheated-air propane flames, designated (a) and (b) respectively. It is clear that the increase in preheated-air temperature significantly increases the magnitude of soot concentrations in composition space. Further to this, the effect of differential diffusion consideration on soot-yield predictions is evident at all axial locations. The non-diffusing soot-particles are transported along the streamlines prior to reaching the burnt-out region of the flow, which explains the observed impact of differential diffusion effects relatively far downstream. In support of these observations, experimental work [56] also revealed that the effects of differential diffusion on temperature and species mass-fractions can also be observed in these downstream locations, although they are more evident at near-nozzle locale.

It can be seen from Fig. 10 that the distribution of soot particles in mixture fraction space develops too slowly when differential diffusion effects are neglected, leading to low soot concentrations in both fuel-rich and fuel-lean stoichiometries. Soot diffusion can also be seen to equally affect predictions in the lean and rich regions either side of stoichiometric. The impact of including differential diffusion is readily seen, with the now steep gradient of soot concentration, and particle redistribution close to

stoichiometric. In their investigations, Kronenburg et al. [18] discovered that the diffusion term, being the first term on the right-hand side of Eqs. 22 and 23, is responsible for this relocation of concentration and subsequent lack of soot depletion via chemical reaction. As a consequence, soot is seen to accumulate over a relatively small area on the rich side of stoichiometric, which in turn results in the increase of soot concentrations in the soot formation regions as observed in Figs. 8 and 9.

4.   Conclusions

A first-order CMC-based soot model has been applied to the calculation of soot levels in turbulent non-premixed flames of different compositions, pressures, and preheated-air temperatures, with one particular aim being the investigation of the influence of differential diffusion of soot particles on predictions. Predictions of soot formation have been validated against the experimental data of Brookes and Moss [4] for atmospheric and 3 atm methane-air flames, and of Nishida and Mukohara [21] for 323 K and 773 K air preheated-air propane flames. On the whole, predictions of the CMC-soot model are in good agreement with experimentally measured soot levels in both sets of flames. However, some discrepancies in the soot level predictions of the two propane flames deserve further investigation. This is currently being undertaken, and includes aspects of the influence of turbulent fluctuations on soot parameters, and the use of a more elaborate soot model.

The increased mixture density and soot precursor species due to increased pressure result in a significantly higher amount of soot in the 3 atm methane flame, which in turn increases the surface growth rate. The CMC-soot model successfully reproduces experimental observations of the effect of pressure on soot volume fraction production and destruction when differential diffusion is accounted for, as reflected by

good agreement with the data in both the soot formation and oxidation zones in the 1 and 3 atm flames. The model, however, under-predicts the peak soot volume fraction in the weakly sooting atmospheric methane flame, even though mixing is adequately described by the k-ε turbulence model. In contrast, results that ignore differential diffusion significantly under-predict soot volume fraction data, both in the atmospheric and 3 atm methane flames. It is suggested that further study of the effects of pressure on soot formation and gas-phase chemistry should involve more detailed mechanisms for soot nucleation and surface growth.

With respect to centre-line temperature predictions, over-prediction and under-prediction occurred in the lower part and in the far-field region of both propane flames, respectively. Although a reasonable representation of temperatures is obtained along the core of both methane flames, indicating that the assumptions of the radiation model employed are satisfactory, the turbulent mixing field derived from Reynolds stress turbulence closures may be required to improve the center-line temperature predictions in propane the flames. Nonetheless, the model produces qualitatively and quantitatively accurate predictions of axial soot concentrations in the 323 K flame when differential diffusion is accounted for. A downstream shift of the soot distribution profile was observed in the higher preheat temperature flame, which leads to under-predictions and over-predictions of soot concentrations in the formation and oxidation zones, respectively. Uncertainties in soot concentration measurements, obtained using probe techniques, or errors in flow field predictions, may be responsible for this shift.

With the inclusion of differential diffusion effects into the calculations, soot volume fraction predictions in the elevated pressure methane and preheated-air propane flames show good to excellent qualitative and quantitative agreement with data, and compare favorably with the results of earlier investigations of these flames that

employed CMC and flamelet approaches. Results therefore support the importance of accounting for the differential diffusion of soot particles in predicting sooting flames, as previously noted by Kronenburg et al. [18].

Given the simplicity and relative accuracy of the model described, it is envisaged that the CMC-based soot model has great potential to be applied in the modelling of soot formation for more complex fuels and combustion geometries. The inclusion of the benzene mechanism in the soot production model has a nominal effect upon predictions due to the chemistry of the fuels being investigated here. Its inclusion does however present a methodology for the extension of the investigation to more complex fuels such as kerosene, and the results of such future work may be of interest to a wide range of industrial end-users.

This paper demonstrates that these approaches, when applied using different sub-models, perform with a similar level of conformity to experimental observation as previously undertaken calculations. The paper then furthers the validation process by extending the models' application not only to atmospheric and high pressure flames, but to flames of different fuels and levels of pre-heat. Also provided is a comprehensive description of theories and techniques applied to aid the reader in further investigations.

6.   References

[1]   McCrain LL, and Roberts WL. Measurements of the soot volume field in laminar diffusion flames at elevated pressures. Combustion and Flame 2005; 140: 60-9.

[2]   Flower WL, and Bowman CT. Soot production in axisymmetric laminar diffusion flames at pressures from one to ten atmospheres. Proceedings of the Combustion Institute 1986; 21: 1115-24.

[3]   Flower WL. The effect of elevated pressure on the rate of soot production in laminar diffusion flames. Combustion Science and Technology 1986; 48: 31-43.

[4]   Brookes SJ, and Moss JB. Measurements of soot production and thermal radiation from confined turbulent jet diffusion flames of methane. Combustion and Flame1999; 116: 49-61.

[5]   Lim J, Gore J, Viskanta R. A Study of the Effects of Air Preheat on the Structure of Methane/Air Counterflow Diffusion Flames. Combustion and Flame 2000; 121: 262-74.

[6]   Fuse R, Kobayashi H, Ju Y, Maruta K, Niioka T. NOx emission from high-temperature air/methane counterflow diffusion flame. International Journal of Thermal Science 2002; 41: 693-8.

[7]   Pope SB. PDF methods in turbulent reacting flows. Progress in Energy and Combustion Science 1985; 11: 119-92.

[8]   Klimenko AYu, Bilger RW. Conditional Moment Closure for turbulent combustion. Progress in Energy and Combustion Science 1999; 25: 595-687.

[9]   Xu J, Pope SB. PDF Calculations of turbulent nonpremixed flames with local extinction. Combustion and Flame 2000; 123: 281-307.

[10]   Demiraydin L, Gass J, Poulikakos D. On the behaviour of a coupled transient flamelet/PDF transport equation model for non-premixed turbulent flames. Combustion Science and Technology 2003; 175: 1729-60.

[11]   Roomina MR, Bilger RW. Conditional Moment Closure (CMC) predictions of a turbulent methane-air jet flame. Combustion and Flame 2001; 125: 1176-95.

[12]   Fairweather M, Woolley RM. First-order conditional moment closure modelling of turbulent, nonpremixed methane flames. Combustion and Flame 2004; 138: 3-19.

[13]   Fairweather M, Woolley RM. First-order conditional moment closure modelling of turbulent, nonpremixed hydrogen flames. Combustion and Flame 2003; 133: 393-405.

[14]   Fairweather M, Woolley RM. Prediction of turbulent non-premixed hydrogen flames using second-order conditional moment closure modelling. Progress in Computational Fluid Dynamics 2006; 6: 158-67.

[15]   Kim IS, Mastorakos E. Simulations of turbulent lifted jet flames with two-dimensional Conditional Moment Closure. Proceedings of the Combustion Institute 2005; 30: 905-12.

[16]   Devaud CB, Bray KNC. Assessment of the applicability of Conditional Moment Closure to a lifted turbulent flame: First order model. Combustion and Flame 2003; 132: 102-14.

[17]   Kim SH, Huh KY, Tao L. Application of the elliptic conditional moment closure model to a two-dimensional nonpremixed methanol bluff-body flame. Combustion and Flame 2000; 120: 75-90.

[18]   Kronenburg A, Bilger RW, Kent JH. Modeling soot formation in turbulent methane-air jet diffusion flames. Combustion and Flame 2000; 121: 24-40.

[19]   Leung KM, Lindstedt RP, Jones WP. A simplified reaction mechanism for soot formation in nonpremixed flames. Combustion and Flame 1991; 87: 289-305.

[20]   Lindstedt RP. In: Bockhorn H, editor. Soot formation in Combustion, Berlin: Springer-Verlag; 1994.

[21]   Nishida O, Mukohara S. Characteristics of soot formation and decomposition in turbulent diffusion flames. Combustion and Flame 1982; 47: 269-79.

[22]   Fairweather M, Jones WP, Ledin HS, Lindstedt RP. Predictions of soot formation in turbulent non-premixed propane flames. Proceedings of the Combustion Institute 1992; 24: 1067-74.

[23]   Jurng J, Shin HD, Lee CK. Predictions of structure with soot concentrations of propane-air turbulent flames. Journal of the Institute of Energy 1988; 155: 201-8.

[24]   Santoro RJ, Semerjian HG, Dobbins RA. Soot particle measurements in diffusion flames. Combustion and Flame 1983; 51: 203-18.

[25]   Kennedy IM. Models of soot formation and oxidation. Progress in Energy and Combustion Science 1997; 23: 95-132.

[26]   Jones WP, Launder BE, The prediction of laminarization with a two equation model of turbulence. International Journal of Heat and Mass Transfer 1972; 15: 301-14.

[27]   Qin Z, Lissianski V, Yang H, Gardiner WC Jr, Davis SG, Wang H. Combustion chemistry of propane: A case study of detailed reaction mechanism optimization. Proceedings of the Combustion Institute 2000; 28: 1663-9.

[28]   Ma G, Wen JZ, Lightstone MF, Thomson MJ. Optimization of soot modelling in turbulent nonpremixed ethylene/air jet flames. Combustion Science and Technology 2005; 177: 1-36.

[29]   Spalding DB. GENMIX: A general computer program for two-dimensional parabolic phenomena, London: Pergamon Press.

[30]   Barlow RS, Carter CD, Relationships among nitric oxide, temperature and mixture fraction in hydrogen jet flames. Combustion and Flame 1996; 104: 288-99.

[31]   Klimenko AY. Multicomponent diffusion of various admixtures in turbulent flow. Fluid Dynamics 1990; 25: 327-4.

[32]   Barlow RS, Smith NSA, Chen J-Y, Bilger RW. Nitric oxide formation in dilute hydrogen jet flames: Isolation of the effects of radiation and turbulence-chemistry submodels. Combustion and Flame 1999; 117: 4-31.

[33]   Girimaji SS. Assumed β-pdf model for turbulent mixing: Validaton and extension to multiple scalar mixing. Combustion Science and Technology 1991; 78: 177-96.

[34]   Kee RJ, Rupley FM, Miller JA. CHEMKIN II: A FORTRAN chemical kinetics package for the analysis of gas-phase chemical kinetics. Sandia National Laboratories 1996; Report No SAND89-8009B.

[35]   Smith GP, Golden DM, Frenklach M, Moriarty NW, Eiteneer B, Goldenberg M, Bowman CT, Hanson RK, Song S, Gardiner WC, Lissianski VV, and Qin Z. http://meberkeleyedu/gri-mech/version30/text30html

[36]   Davis SG, Law CK, Wang H. Propene pyrolysis and oxidation kinetics in a flow reactor and laminar flames. Combustion and Flame 1999; 119: 375-99.

[37]   Miller JA, Bowman CT. Mechanism and modelling of nitrogen chemistry in combustion. Progress in Energy and Combustion Science 1989; 15: 287-338.

[38]   Marracino B and Lentini D. Radiation modelling in non-luminous nonpremixed turbulent flames. Combustion Science and Technology 1997; 128: 23-48.

[39]   Widmann JF. Evaluation of the Plank mean absorption coefficients for radiation transport through smoke. Combustion Science and Technology 2003; 175: 2299-308.

[40]   Brown PN, Byrne GD, Hindmarsh AC. VODE, a variable-coefficient ODE solver. SIAM Journal on Scientific and Statistical Computing 1989; 10: 1038-51.

[41]   Frenklach M, Wang H. In: Bockhorn H, editor. Soot formation in combustion, Berlin: Springer-Verlag; 1994.

[42]   Kazakov A, Frenklach M. Soot particle coagulation and aggregation. Combustion and Flame 1998; 114: 484-501.

[43]   Wen JZ, Thomson M, Park S, Rogak S, Lightstone M. Study of soot growth in a plug flow reactor using a moving sectional model. Proceedings of the Combustion Institute 2005; 30: 1477-84.

[44]   Moss BJ. In: Bockhorn H, editor. Soot formation in combustion, Berlin: Springer-Verlag; 1994.

[45]   Young KJ and Moss JB. Modelling sooting turbulent jet flames using an extended flamelet technique. Combustion Science and Technology 1995; 105: 33-53.

[46]   Stanmore BR, Brilhac JF, Gilot P. The oxidation of soot: a review of experiments, mechanism and models. Carbon 2001; 39: 2247-68.

[47]   Haynes BS, Jander H, Wagner HG. The effect of metal additives on the formation of soot in premixed flames. Proceedings of the Combustion Institute 1979; 17: 1365-74.

[48]   Kronenburg A, Bilger RW. Modelling differential diffusion in nonpremixed reacting turbulent flow: Application to turbulent jet flames. Combustion Science and Technology 2001; 166: 175-94.

[49]   Kronenburg A, Bilger RW. Modelling differential diffusion in nonpremixed reacting turbulent flow: Model development. Combustion Science and Technology 2001; 166: 195-227.

[50]   Mauss F, Netzell K, Lehtiniemi H. Aspects of modelling soot formation in turbulent diffusion flames. Combustion Science and Technology 2006; 178: 1871-85.

[51]   Roditcheva OV, Bai XS. Pressure effect on soot formation in turbulent diffusion flames. Chemosphere 2001; 42: 811-21.

[52]   Brookes SJ, Moss JB. Predictions of soot and thermal radiation properties in confined turbulent jet diffusion flames. Combustion and Flame 1999; 116: 486-503.

[53]   Liu F, Thomson KA, Guo H, Smallwood GJ. Numerical and experimental study of an axisymmetric coflow laminar methane–air diffusion flame at pressures between 5 and 40 atmospheres. Combustion and Flame 2006; 146: 456-471.

[54]   Zhang Z, Ezekoye OE. Soot production rate calculations at elevated pressure in a methane-air jet diffusion flame. Combustion Science and Technology 1998; 137: 323-46.

[55]   Coelho PJ, Carvalho MG. Modeling of soot formation and oxidation in turbulent diffusion flames. Journal of Thermophysics and Heat Transfer 1995; 9: 644-52.

[56]   Bergmann V, Meier W, Wolff D, Stricker W, Application of spontaneous Raman and Rayleigh scattering and 2D LIF for the characterization of a turbulent $CH_4/H_2/N_2$ jet diffusion flame. Applied Physics B 1998; 66: 489-502.

Table 1. Operating conditions for methane elevated pressure flames.

Flame operating pressure	1 atm	3 atm
Fuel mass flow (gmin^{-1})	10.3	10.3
Air mass flow (gmin^{-1})	708	708
Fuel temperature (K)	290	290
Air temperature (K)	290	290
Fuel jet velocity (m s^{-1})	20.3	6.77
Exit Reynolds number	5000	5000

Table 2. Operating conditions for preheated-air propane flames.

Air exit temperature (K)	323	773
Absolute pressure (atm)	1	1
Fuel exit velocity (m s^{-1})	30.0	30.0
Fuel exit temperature (K)	298	298
Nozzle diameter (mm)	2.0	2.0
Exit Reynolds number	13000	13000
Co-flow air velocity (ms^{-1})	0.4	0.96

Table 3. Reaction rate constants for soot formation and oxidation, in the form of the

Arrhenius expression $k_j = AT^b \exp(-T_a/T)$ (units K, kmol, m, s).

k_j	A	b	T_a	References
k_1	$1.0 \cdot 10^4$	0	21,000	[20, 22]
k_2	$0.75 \cdot 10^5$	0	21,000	[20]
k_3	$0.75 \cdot 10^3$	0	12,100	[20]
k_4	$7.15 \cdot 10^2$	0.5	19,680	[22]
k_5	$3.6 \cdot 10^{-1}$	0.5	0	[18]
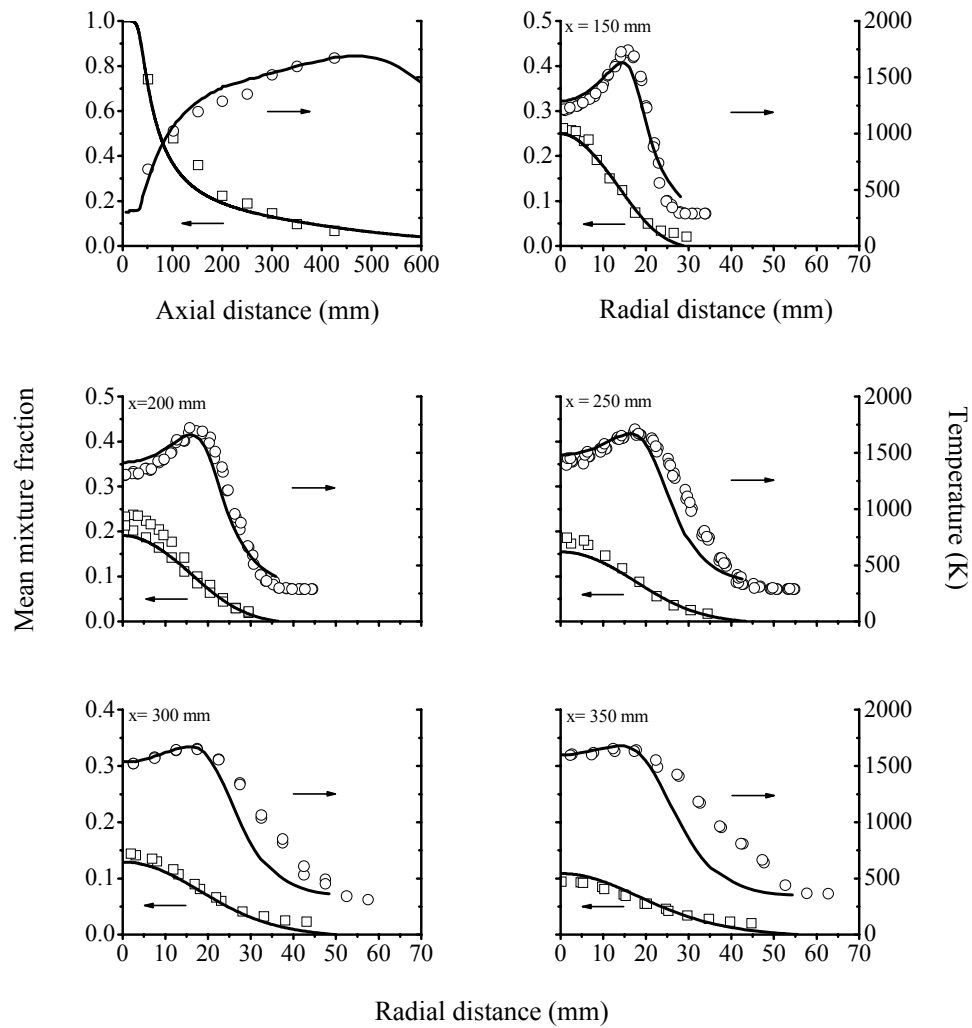
Figure 1. Axial and radial mean mixture fraction and temperature predictions plotted against experimental data for the 1 atm methane flame (symbol – measured, line – predicted).
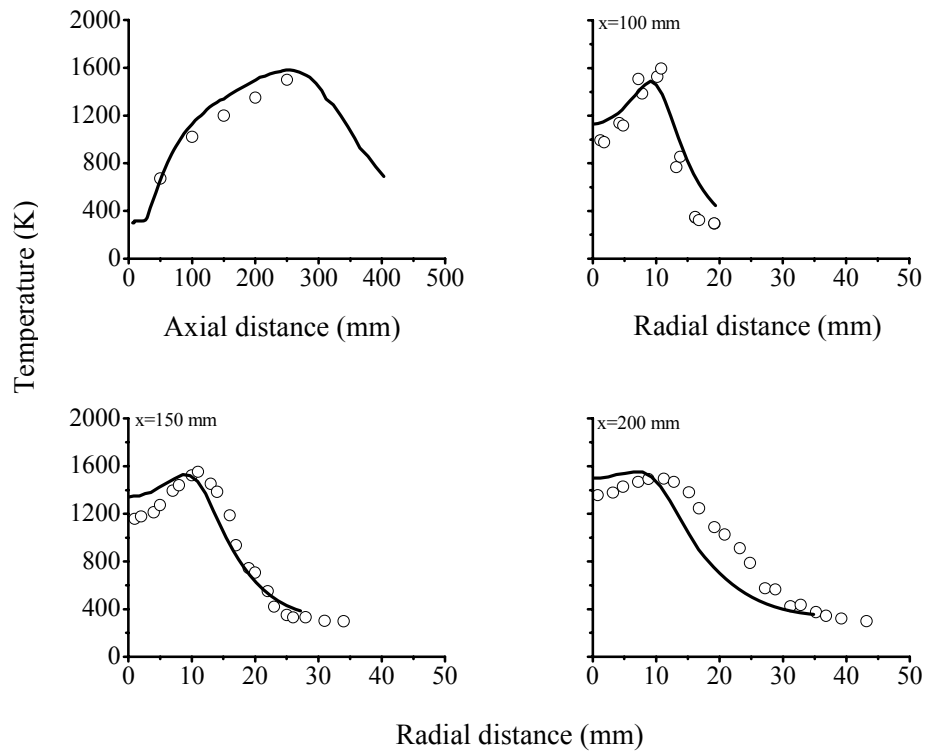
Figure 2.   Axial and radial temperature predictions plotted against experimental data for the 3 atm methane flame (symbol – measured, line – predicted).
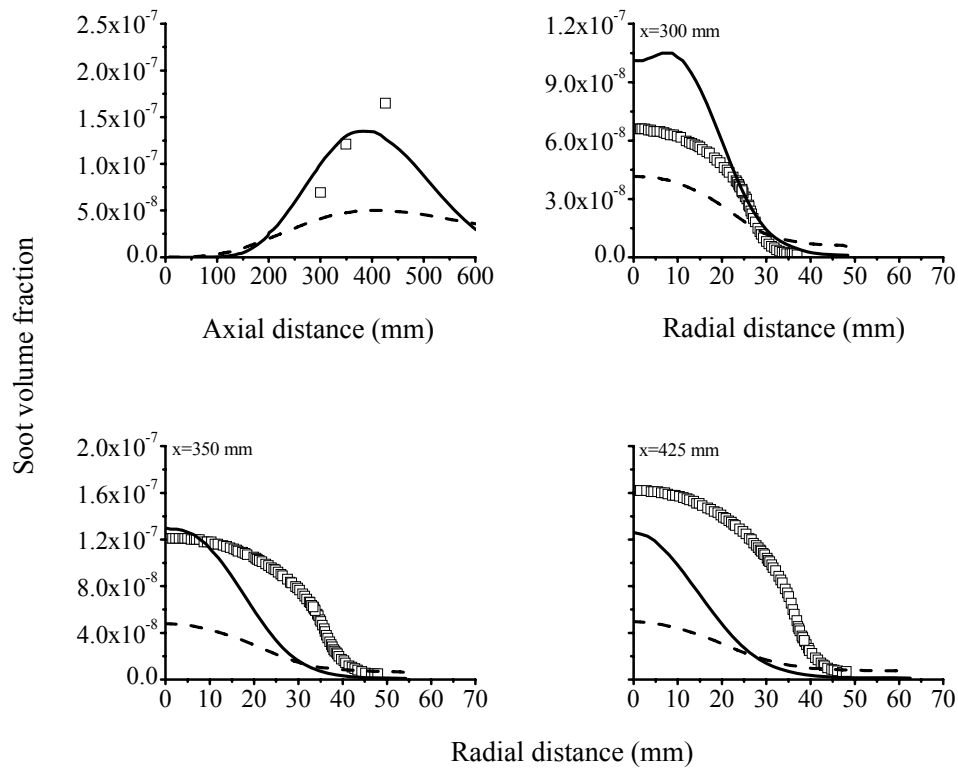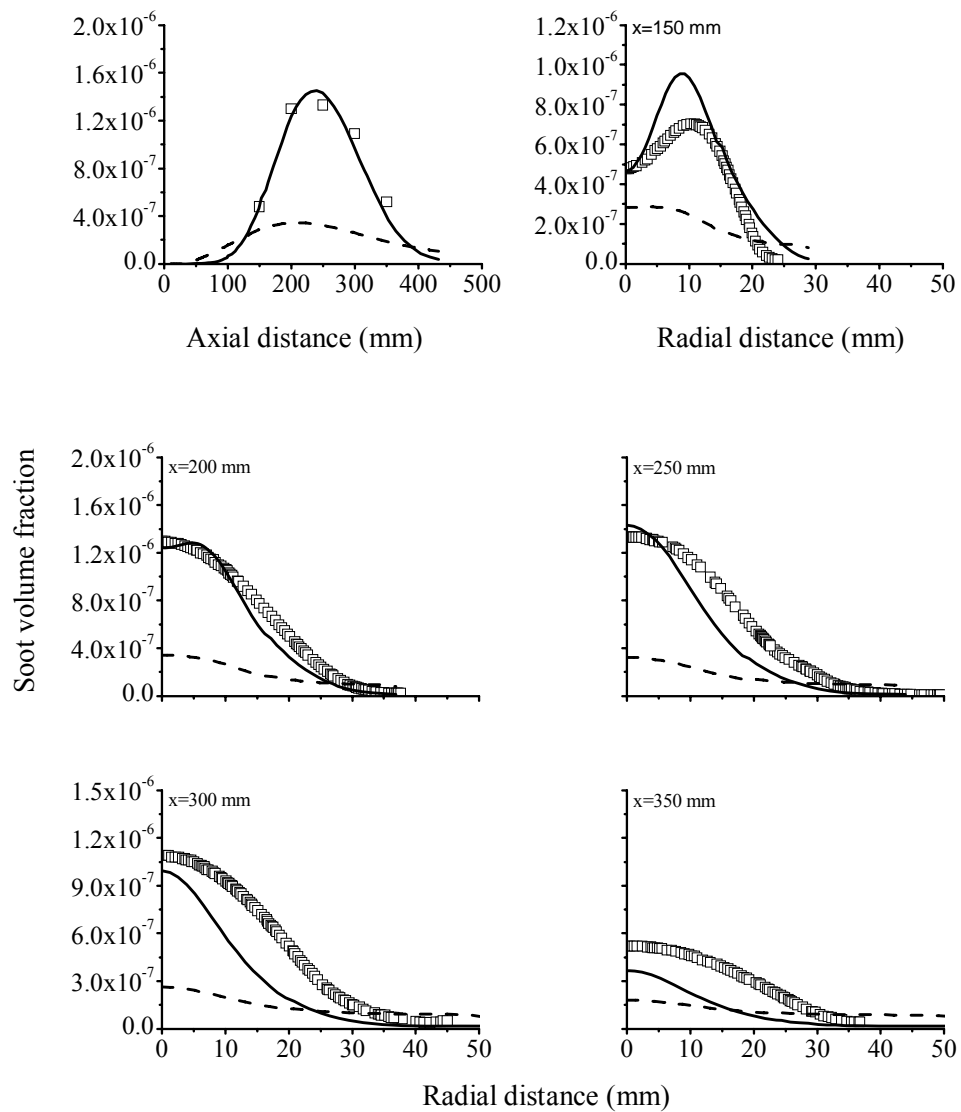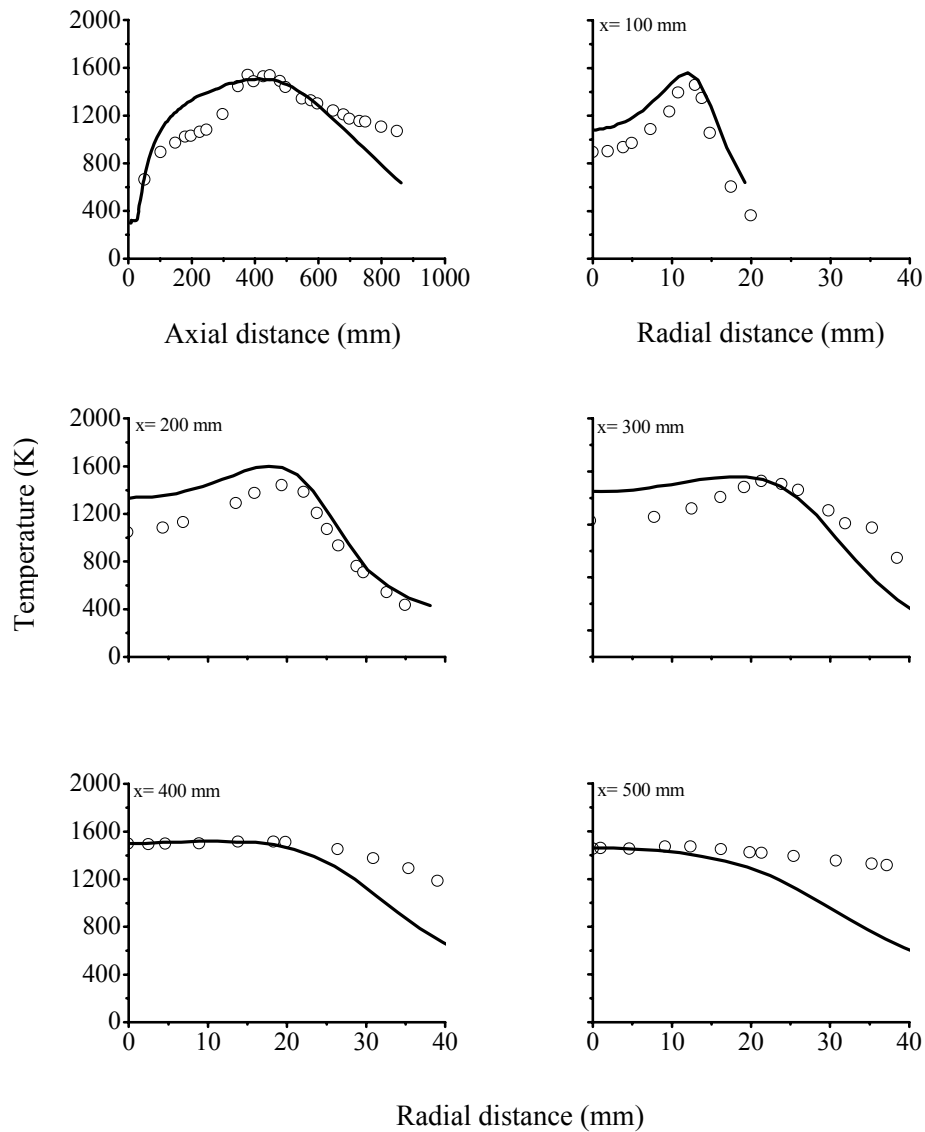
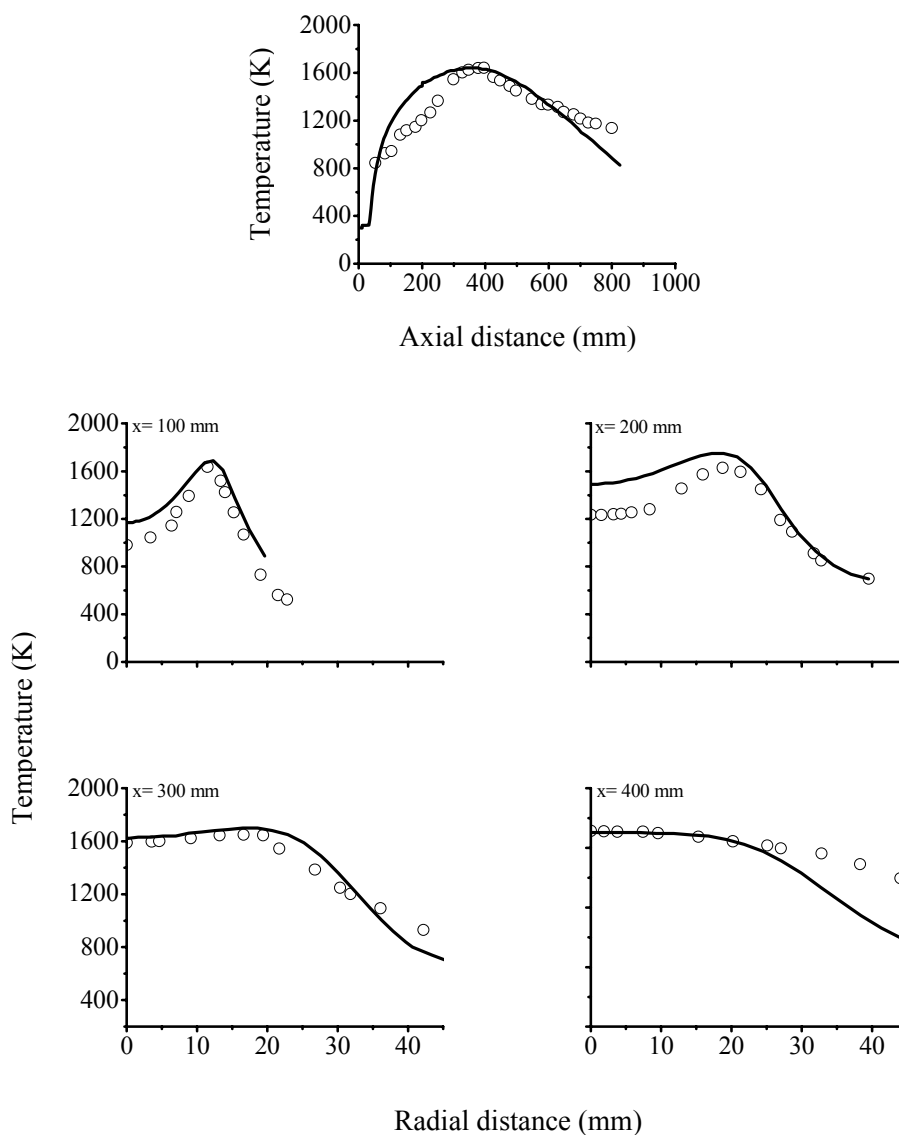**Figure 3.**   Axial and radial soot volume fraction predictions plotted against experimental data for the 1 atm methane flame (symbol – measured, solid line – predicted with differential diffusion, dashed line – predicted neglecting differential diffusion).

Figure 4. Axial and radial soot volume fraction predictions plotted against experimental data for the 3 atm methane flame (symbol – measured, solid line – predicted with differential diffusion, dashed line – predicted neglecting differential diffusion).
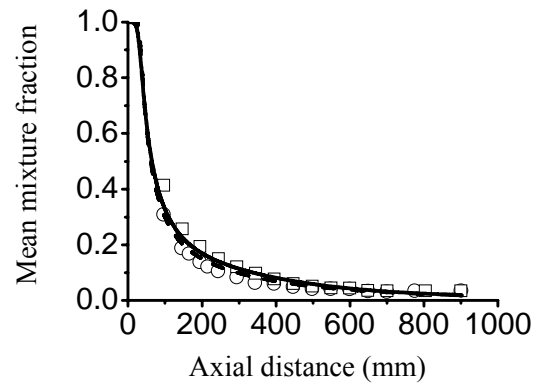
Figure 5. Axial mean mixture fraction predictions plotted against experimental data for the 323 K (○) and 773 K (□) preheated-air propane flames (dashed line – predicted 323 K flame, solid line – predicted 773 K flame).

Figure 6. Axial and radial temperature predictions plotted against experimental data for the 323 K preheated-air propane flame (symbol – measured, line – predicted).

Figure 7. Axial and radial temperature predictions plotted against experimental data for the 773 K preheated-air propane flame (symbol – measured, line – predicted).
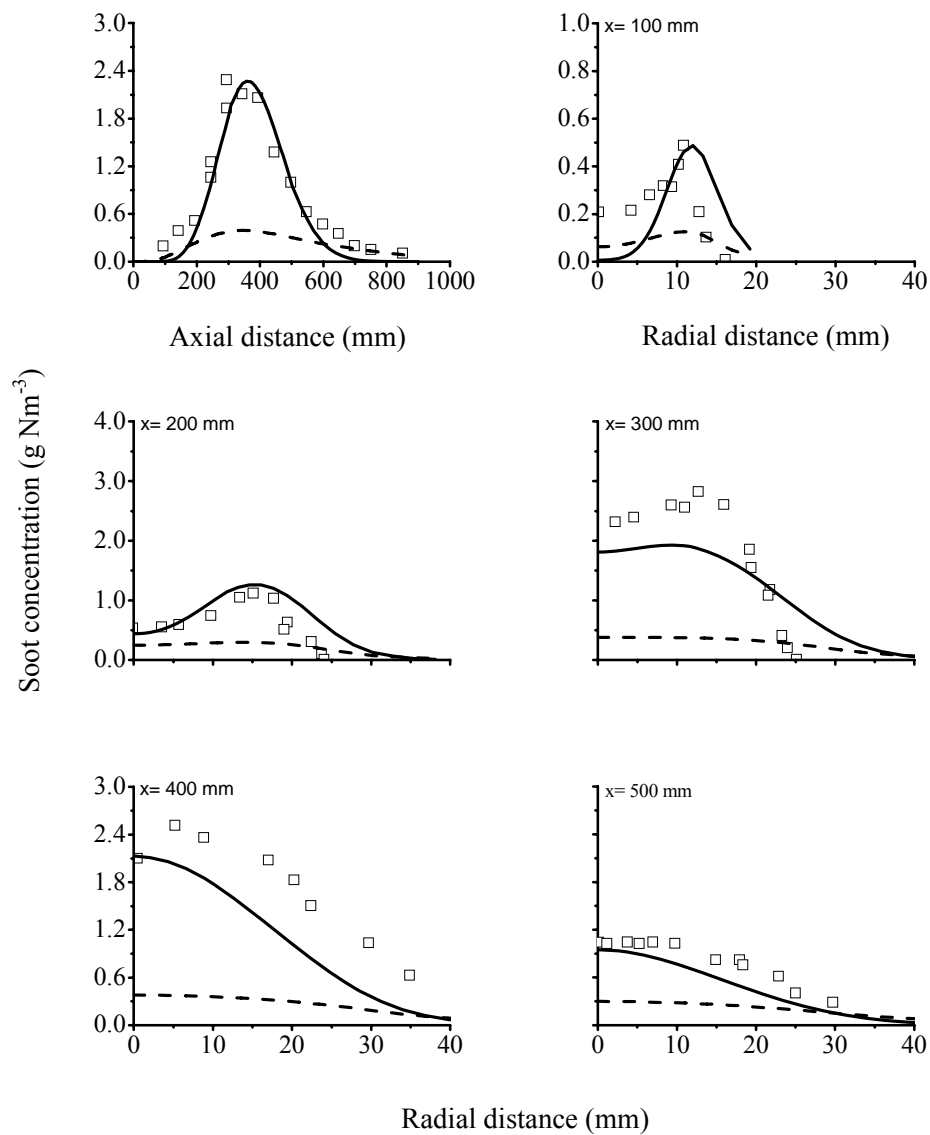
Figure 8. Axial and radial soot concentration predictions plotted against experimental data for the 323 K preheated-air propane flame (symbol – measured, solid line – predicted with differential diffusion, dashed line – predicted neglecting differential diffusion).
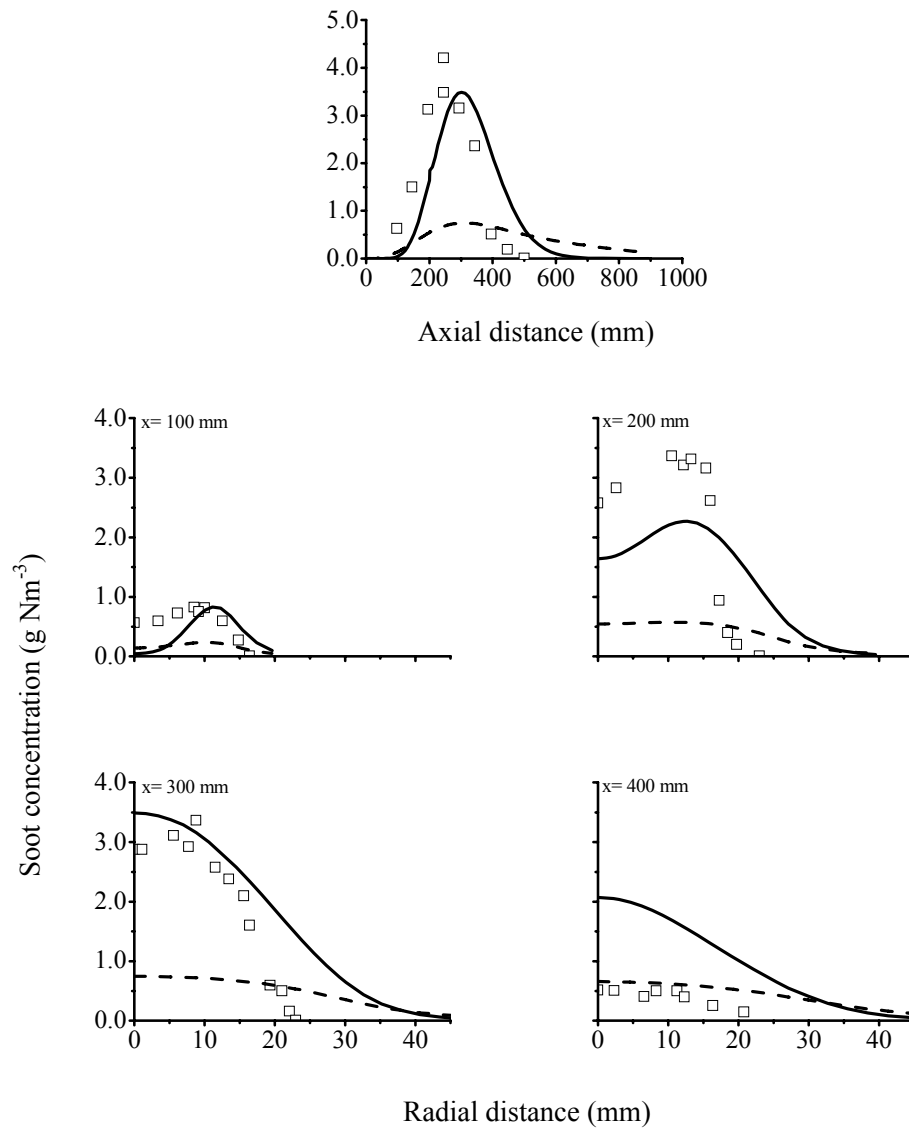
Figure 9. Axial and radial soot concentration predictions plotted against experimental data for the 773 K preheated-air propane flame (symbol – measured, solid line – predicted with differential diffusion, dashed line – predicted neglecting differential diffusion).
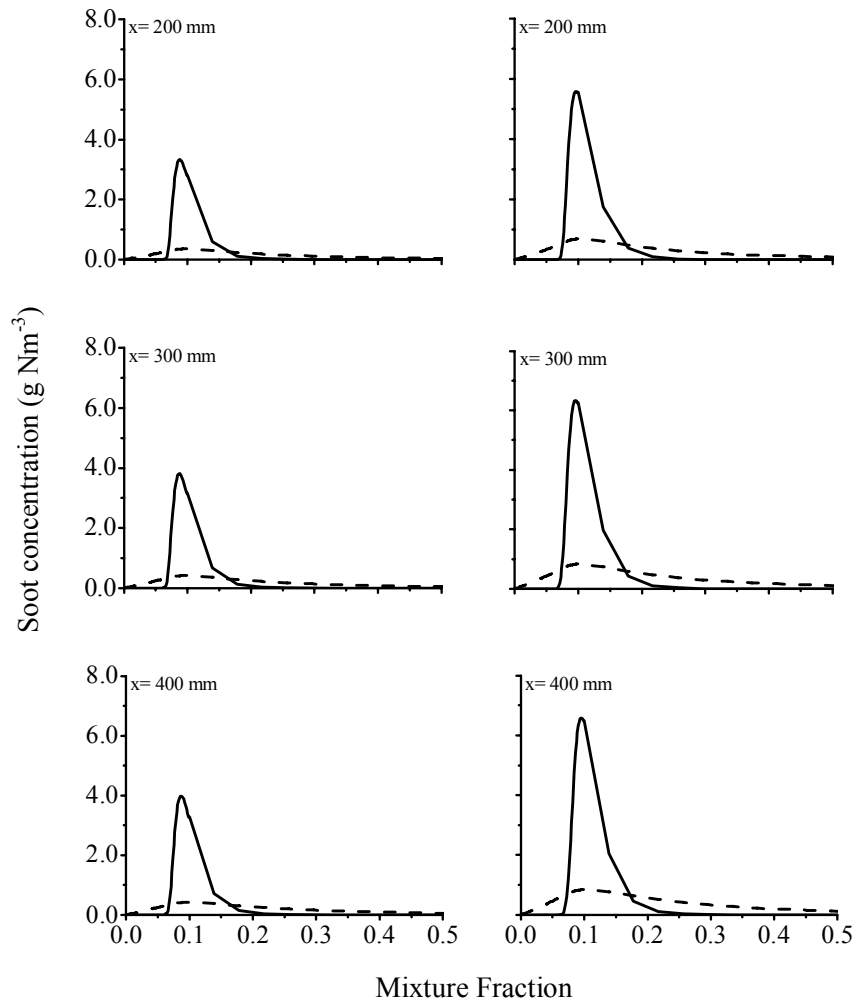
Figure 10. Soot concentrations in mixture fraction space at x = 200, 300, and 400 mm for the 323 K (a) and 773 K (b) preheated-air propane flames (solid line – predicted with differential diffusion, dashed line – predicted neglecting differential diffusion).